Laser Flash Photolysis Studies of Radical−Radical Reaction Kinetics: The HO_2 + IO Reaction

J. M. Cronkhite,[†] R. E. Stickel,[‡] J. M. Nicovich,[§] and P. H. Wine*[,‡,§]

School of Physics, School of Earth and Atmospheric Sciences, and School of Chemistry and Biochemistry, Georgia Institute of Technology, Atlanta, Georgia 30032

Received: January 8, 1999; In Final Form: March 1, 1999

Laser flash photolysis of $Cl_2/CH_3OH/O_2/I_2/NO_2/SF_6/N_2$ mixtures at 308 nm has been coupled with simultaneous time-resolved detection of HO_2 (by infrared tunable diode laser absorption spectroscopy) and IO (by visible absorption spectroscopy) to investigate the kinetics of the atmospherically important reaction HO_2 + IO → products over the temperature range 274−373 K in N_2 buffer gas at pressures of 12 and 25 Torr. All experiments were performed under near pseudo-first-order conditions with HO_2 in excess over IO. At 298 K, the rate coefficient was determined to be $(9.7 \pm 2.9) \times 10^{-11}$ cm^3 molecule^{-1} s^{-1}, with the primary source of uncertainty being knowledge of the infrared line strength(s) required to convert measured HO_2 absorbances to absolute concentrations. The temperature dependence of the HO_2 + IO rate coefficient was found to be adequately described by the Arrhenius expression $k = 9.3 \times 10^{-12} \exp(680/T)$ cm^3 molecule^{-1} s^{-1}. The results reported in this study are compared with other recent studies of HO_2 + IO kinetics, and the potential roles of this reaction in atmospheric chemistry are discussed.

Introduction

Reactive iodine as a potential tropospheric O_3 sink has received considerable attention recently.[1−3] Because organic iodine compounds photolyze readily in the troposphere, known source gases such as CH_3I can easily be converted to reactive IO radicals, e.g.,

$$CH_3I + h\nu \rightarrow CH_3 + I \quad (1)$$

$$I + O_3 \rightarrow IO + O_2 \quad (2)$$

Moreover, the photolytic instability of potential iodine reservoirs (i.e., HOI, $IONO_2$, HI, etc.) in the troposphere allows iodine to preferentially reside in its catalytically reactive forms, i.e., I and IO. Tropospheric iodine can participate in catalytic ozone destruction cycles analogous to those involving chlorine and bromine in the stratosphere. One important example is

$$IO + HO_2 \rightarrow HOI + O_2 \quad (3)$$

$$HOI + h\nu \rightarrow OH + I \quad (4)$$

$$I + O_3 \rightarrow IO + O_2 \quad (2)$$

$$OH + O_3 \rightarrow HO_2 + O_2 \quad (5)$$

$$\text{net: } 2O_3 \rightarrow 3O_2$$

Sources of atmospheric organic iodine include CH_3I and other iodocarbons (e.g., CH_2ICl, CH_2I_2, C_2H_5I) released from the oceans and from biomass burning.[1,4] Recent field experiments have detected CH_3I in the middle and upper troposphere at concentrations that imply total iodine abundances sufficient to significantly impact total column ozone, as well as HO_2/OH concentration ratios.[3]

It has recently been suggested that iodine may also play a significant role in stratospheric ozone depletion.[4] Although iodine source compounds analogous to the chloro- and bromocarbons have short tropospheric lifetimes toward photolysis, strongly convective storm systems in the tropics may be capable of rapidly transporting such species to the upper troposphere and lower stratosphere.[3−6] As mentioned above, iodine reservoir species are less photolytically stable than their bromine or chlorine analogues, rendering iodine correspondingly more efficient as an ozone removal catalyst. Reaction 3 acting as part of the above catalytic cycle could contribute significantly to lower stratospheric ozone loss given sufficient stratospheric iodine levels.[4] Solomon et al.[4] estimated that the ozone loss frequency via the IO + HO_2 cycle at an altitude of 14 km is equal to 60% of that due to chlorine, assuming a rate coefficient of $k_3 = 6.4 \times 10^{-11}$ cm^3 molecule^{-1} s^{-1} [7] and a lower stratospheric iodine abundance of 1 pptv.

Two reports of the IO + HO_2 rate coefficient measured at room temperature have appeared in the literature; Jenkin et al.[7] used the molecular modulation technique to obtain $k_3 = 6.4 \times 10^{-11}$ cm^3 molecule^{-1} s^{-1}, and Maguin et al.[8] employed a low-pressure discharge-flow/mass spectrometry technique and obtained $k_3 = 1.04 \times 10^{-10}$ cm^3 molecule^{-1} s^{-1}. No temperature-dependent studies of IO + HO_2 kinetics have been published to date.

In this paper, we report a study of the temperature-dependent kinetics of the HO_2 + IO reaction. Whereas a majority of direct studies of radical−radical reaction kinetics employ discharge flow techniques, the present study uses flash photolysis methodology. Comparison of kinetic data obtained using very different experimental methods is one useful means for elucidating systematic errors in the different experimental approaches. The kinetic data reported in this paper are discussed in light of

* To whom correspondence should be addressed.
[†] School of Physics; present address: Physical and Chemical Properties Division, National Institute of Standards and Technology, 100 Bureau Drive, Stop 8381, Gaithersburg, Maryland 20899-8381.
[‡] School of Earth and Atmospheric Sciences.
[§] School of Chemistry and Biochemistry.

10.1021/jp990135v CCC: $18.00
Published on Web 04/10/1999

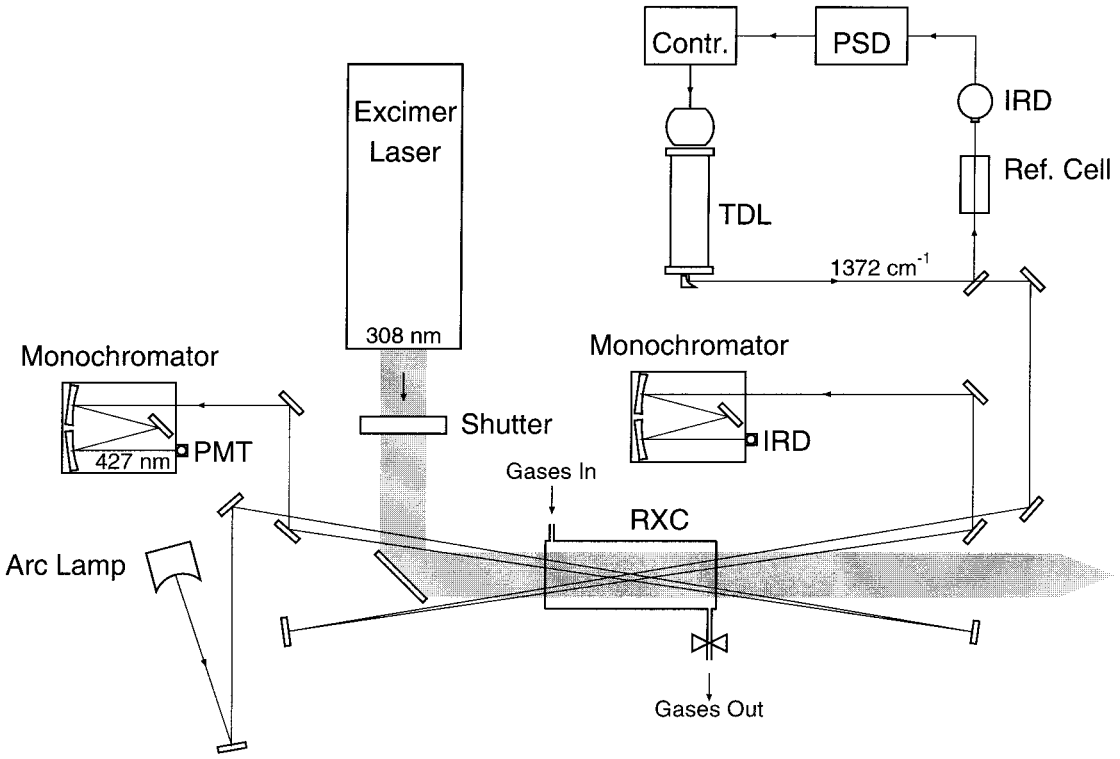

Figure 1. Schematic diagram of the experimental apparatus. Contr. = controller; IRD = infrared detector; PMT = photomultiplier tube; PSD = phase-sensitive detector; Ref. = reference; RXC = reaction cell.

current understanding of atmospheric iodine chemistry and previously reported room-temperature results.

Experimental Technique

The kinetics of the HO_2 + IO reaction were investigated by 308 nm pulsed laser photolysis of $N_2/O_2/CH_3OH/Cl_2/NO_2/SF_6/I_2$ mixtures, using an approach that is very similar to one we have employed previously to study HO_2 + BrO kinetics at 298 K.[9] The experiments were conducted at 12 Torr and room temperature and 25 Torr at four different temperatures. In all experiments, HO_2 was maintained in excess (typically a factor of 10) over IO. Absolute IO and HO_2 concentrations were simultaneously monitored in situ in a time-resolved fashion. IO was monitored using longpath visible absorption spectroscopy; HO_2 was monitored using infrared tunable diode laser absorption spectroscopy (TDLAS).

HO_2 radicals were generated via the reaction scheme

$$Cl_2 + h\nu(308\ \text{nm}) \rightarrow 2\ Cl(^2P_J) \quad (6)$$

$$Cl(^2P_J) + CH_3OH \rightarrow CH_2OH + HCl \quad (7)$$

$$CH_2OH + O_2 \rightarrow HO_2 + CH_2O \quad (8)$$

which produced peak HO_2 concentrations of $(19-73) \times 10^{12}$ molecules cm^{-3} under the conditions employed. IO radicals at peak concentrations in the range $(1.6-5.4) \times 10^{12}$ molecules cm^{-3} were simultaneously generated via

$$NO_2 + h\nu(308\ \text{nm}) \rightarrow O(^3P_J) + NO \quad (9)$$

$$I_2 + O(^3P_J) \rightarrow IO + I(^2P_J) \quad (10)$$

HO_2 and IO were generated on a time scale much shorter than the time scale for their removal under the experimental conditions employed. HO_2 generation was complete within a few microseconds after the laser flash; IO formation was essentially complete within 50 μs.

A schematic of the experimental apparatus is shown in Figure 1. A sealed glass-jacketed reaction cell with inlet and outlet ports allowed temperature control via circulation of thermostated fluid through the jacket. A 3.5 cm × 1.0 cm mask on the entrance and exit windows defined the region over which the photolysis beam and the visible and IR detection beams overlapped. The reagent gas mixture was flowed through the reaction cell at a linear flow velocity of 4−8 cm s^{-1} with a laser flash repetition rate of 0.125−0.25 Hz; this allowed for replenishment of the reagents between laser flashes, thus preventing accumulation of the reaction and photolysis products in the reactor. The photolysis laser beam measured approximately 4 cm × 1.5 cm in cross section at its entrance to the reaction cell and typically delivered an energy density of 40−50 mJ per cm^2 per pulse over this area in pulses of ≈20 ns duration. It entered and exited the reaction cell nearly collinearly with the visible and IR detection beams and was then deflected after exiting the cell to an absorbing medium to prevent unintended reflections and scatter. The laser pulse energy was monitored continuously using the internal energy meter of the laser (Lambda Physik Lextra 200); an absolute calibration was obtained using a thermopile calorimeter energy meter (Scientech model 38-0105) at least once per day. The energy thus measured was corrected for window losses (measured to be <10%) and reflections within the cell to derive an estimate of the laser pulse energy in the reaction zone. Shot-to-shot laser pulse energy variations were less than 2% on average, and the cross-sectional spatial intensity variations in the photolysis beam were measured to be less than 10% for the portion of the beam which irradiated the detection volume. Because (1) the reaction cell length along the photolysis axis was only 30 cm and (2) the beam traveled several meters before entering the reaction cell, beam divergence through the photolysis region was expected to be minimal. This

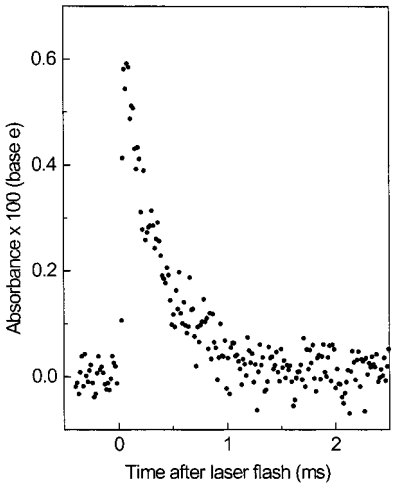

Figure 2. Observed absorbance temporal profile at 427.2 nm under the conditions of experiment 6 (Table 3). Number of laser shots averaged = 125.

was confirmed by measurements of laser fluence as a function of position with the cell removed from the beam path.

IO radicals were detected using time-resolved visible absorption spectroscopy at 427.2 nm, the peak of the strong 4-0 band of the $A^2\Pi_{3/2}-X^2\Pi_{3/2}$ transition of IO, for which the peak absorption cross section has been measured by Harwood et al.[10] to be $(3.6 \pm 0.5) \times 10^{-17}$ cm^2 molecule^{-1}, independent of temperature in the 203−373 K range. Because of the difference in resolution employed between the cross section measurements of Harwood et al. and the absorption measurements described here, for the purpose of the present measurements a 10% correction was applied to their reported cross section based on their high-resolution data for the (4,0) band shape (i.e., convolution of a triangular slit function with the band shape at the monitored wavelength). The output from a 150 W high-pressure xenon arc lamp was employed as the light source for IO detection. After optical collimation, the beam was passed twice through the photolysis region of the reaction cell nearly collinearly with the 308 nm photolysis beam and then passed through a 0.22 m monochromator tuned to 427.2 nm (resolution 0.30 nm) to isolate the desired wavelength. A photomultiplier tube (PMT) monitored the light level. The time-dependent current output of the PMT was sent through a fixed resistor, and the resulting voltage was monitored and stored by a digital signal averager with 8-bit voltage resolution. A 25 μs *RC* time constant for the resistor/PMT circuit was chosen to give adequate temporal resolution for the observed time scale of the IO decays.

Data acquisition was pretriggered relative to the laser flash to obtain I_0, the 427.2 nm light level prior to IO production. The IO absorption cross section at 427.2 nm was used to convert measured IO absorbances to absolute concentrations using the Beer−Lambert law,

$$[\mathrm{IO}] = \frac{\ln(I_0/I_t)}{\sigma_{\mathrm{IO}}\, l} \qquad \text{(I)}$$

where I_t is the 427.2 nm light level at a time t after the laser flash, σ_{IO} is the IO absorption cross section, and l is the absorption path length. A typical 427.2 nm absorbance temporal profile is shown in Figure 2. The somewhat lower than desirable signal-to-noise ratio for IO detection results from the facts that (a) chemistry considerations dictated that the IO concentration be kept reasonably low and (b) the requirements that three laser beams overlap, that the absorption path lengths for IO and

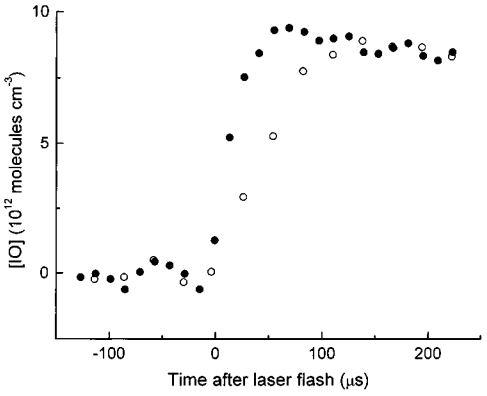

Figure 3. Effect of SF_6 on the observed IO appearance rate in the absence of HO_2. ○, $[SF_6] = 0$; ●: $[SF_6] = 3 \times 10^{16}$ per cm^3.

(particularly) HO_2 be well defined, and that the concentrations be reasonably uniform over the absorption path lengths dictated that the path length be relatively short, i.e., 60 cm. The IO detection sensitivity in a typical experiment was 2.5×10^{11} per cm^3 (defined as the concentration where a signal-to-noise ratio of unity could be obtained by averaging 100 laser shots).

Initial experiments to examine IO production and decay in a $NO_2/I_2/N_2$ mixture showed that the appearance rate of IO detected using 427.2 nm absorption was significantly slower than expected based on the rate coefficient for reaction 10 recommended by DeMore et al.,[11] i.e., 1.4×10^{-10} cm^3 molecule^{-1} s^{-1}. To explain this observation, it was hypothesized that IO was being produced in vibrationally excited states from reaction 10 and subsequently deactivated at a rate comparable to or slower than the rate for reaction 10 under the conditions employed. Because the detection method used was only sensitive to IO in its lowest vibrational level, this could potentially account for the observed behavior. To test this hypothesis, SF_6 was added to deactivate vibrationally excited IO, i.e.,

$$\mathrm{SF_6} + \mathrm{IO}(v \geq 1) \rightarrow \mathrm{SF_6} + \mathrm{IO}(v = 0) \qquad (11)$$

Upon addition of 1 Torr SF_6, the observed IO production rate fell into good agreement with that predicted by reaction 10 alone (see Figure 3). SF_6 was added to the gas mixture to deactivate vibrationally excited IO in all of the HO_2 + IO rate coefficient experiments.

HO_2 radicals were detected via time-resolved IR tunable diode laser (TDL) absorption at 1371.927 cm^{-1}, the center of a nearly coincident pair of strong HO_2 rovibrational absorption lines with a combined integrated line strength of $(1.2 \pm 0.3) \times 10^{-20}$ cm^2 molecule^{-1} cm^{-1} at 296 K.[12] The output from a Pb salt IR TDL (Laser Photonics L5600) was optically collimated and passed twice through the photolysis region of the reaction cell nearly collinearly with the 308 nm photolysis beam, giving an absorption path length of 61.6 cm. The IR beam was then passed through a 0.5 m monochromator (to isolate the desired TDL mode) to a HgCdTe detector cooled to 77 K, which converted the instantaneous detected IR power level to a voltage. The detector output was monitored by an 8-bit digital signal averager for digitization, storage, and further analysis.

The TDL was frequency modulated at 4 kHz over a narrow spectral region surrounding 1371.927 cm^{-1}. A portion of the output beam was picked off and passed through a reference cell

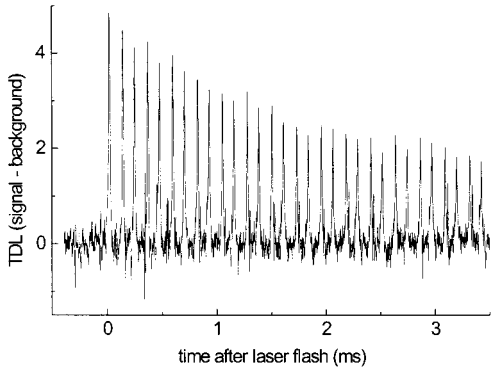

Figure 4. Plot of TDL signal minus baseline as a function of time for experiment 6 (Table 3).

containing CH_3Cl (which has an IR absorption line nearly coincident with the HO_2 line being used) and then to a second IR detector. The output from this detector was used to generate a phase-dependent feedback signal to keep the modulation region centered around the CH_3Cl absorption line (and hence, the HO_2 line as well). Absolute HO_2 concentrations were determined from the integrated line strength at 1371.927 cm^{-1} reported by Zahniser et al.[12] A plot of a typical TDL data set is shown in Figure 4. Integrated absorption was determined by numerical integration of the area under the HO_2 peaks in the digitized temporal profile using

$$S = \frac{1}{nl}\int \ln\frac{I_0}{I(\nu)}\,d\nu = \frac{1}{nl}\int \ln\frac{I_0}{I_0 - y(\nu)}\,d\nu \qquad \text{(II)}$$

where S is the integrated line strength, n is the HO_2 number density, l is the absorption path length, I_0 and $I(\nu)$ are the absolute detected IR signal levels before and after HO_2 production, respectively, and $y(\nu)$ is the detected signal deviation from the zero-absorbance baseline. The results were then calibrated to peak absorption at each pressure employed, so that peak absorbance could be used as a proxy for total absorbance. The absolute baseline IR intensity at the detector, I_0, was determined either by mechanically chopping the beam at 1 kHz or by inference from the measured integrated absorbance of a known concentration of SO_2 at 1371.934 cm^{-1} ($[SO_2]$ was measured in situ using UV photometry at 253.7 nm); the two methods agreed to within 5%. A typical measured HO_2 concentration temporal profile is shown in Figure 5.

Two secondary checks of the absolute HO_2 concentration were also available in this experiment. One was to observe the temporal profile of HO_2 in the absence of I_2/NO_2 to determine the HO_2 loss rate. Under these conditions, HO_2 loss is determined solely (aside from very slow background losses) by the reaction

$$HO_2 + HO_2 \rightarrow H_2O_2 + O_2 \qquad (12)$$

The HO_2 concentration is then related to the rate coefficient for reaction 12 via

$$1/[HO_2]_t = 1/[HO_2]_0 + 2k_{12}t \qquad \text{(III)}$$

where $[HO_2]_0$ is the peak HO_2 concentration, $[HO_2]_t$ is the HO_2 concentration at a time t past the peak, and k_{12} is the rate coefficient for reaction 12. The $[HO_2]$ absorbance data were calibrated so that a linear least-squares fit of the $[HO_2]_t^{-1}$ vs. t data gave the literature value for $2k_{12}$ (2.4×10^{-12} cm^3 $molecule^{-1}$ s^{-1} at 296 K)[11] as the slope at each of the two pressures employed (the pressure-dependent component of k_{12} accounts for only 1−2% of the total rate coefficient in the 12−25 Torr pressure range). This procedure results in HO_2 concentrations that are a factor of 1.05 ± 0.10 (2σ, precision only) times larger than concentrations deduced from the 1372 cm^{-1} absorption line strength calibrations.

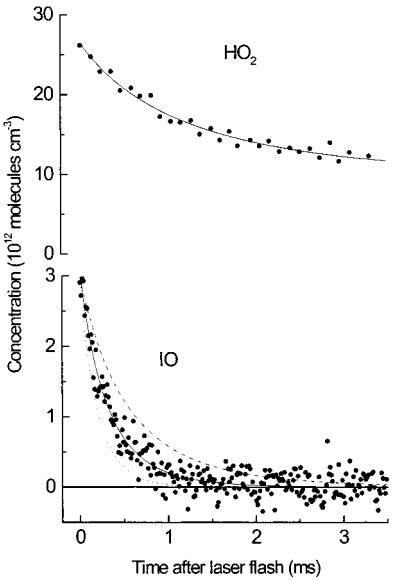

Figure 5. Measured and simulated HO_2 and IO temporal profiles generated from numerical integration of the rate equations using the chemical mechanism given in Table 1. Conditions are those of experiment 6 (Table 3). Points are measured data. Solid line, $k_3 = 10.3 \times 10^{-11}$ cm^3 $molecule^{-1}$ s^{-1} (best fit); dotted line, simulation with $k_3 = 20 \times 10^{-11}$ cm^3 $molecule^{-1}$ s^{-1}; dashed line, simulation with $k_3 = 5.0 \times 10^{-11}$ cm^3 $molecule^{-1}$ s^{-1}.

Another check on absolute $[HO_2]$ was based on Cl atom titration. $[HO_2]$ produced in the absence of I_2/NO_2 is nearly identical to [Cl] produced from Cl_2 photolysis, i.e., the chlorine atoms are completely titrated to HO_2 via reactions 7 and 8. $[Cl]_0$, the chlorine atom concentration initially produced by the laser flash, was determined from

$$[Cl]_0 = 2[Cl_2]E(\sigma\lambda/hc) \qquad \text{(IV)}$$

where $[Cl_2]$ is the molecular chlorine concentration prior to the laser flash, E is the laser pulse energy per unit area, σ is the 308 nm absorption cross section for Cl_2, λ is the laser wavelength, h is Planck's constant, and c is the speed of light. This $[HO_2]$ determination method gave results in excellent agreement with the two aforementioned methods within the estimated uncertainty, which is primarily due to spatial variations in the photolysis beam intensity and uncertainty in the Cl_2 concentration. Both secondary checks on HO_2 concentrations were carried out for each value of $[HO_2]$ investigated.

Temperature corrections for the HO_2 line strength were calculated on the basis of data compiled in the HITRAN 1996 database[13] and using software provided with the database for calculating the partition function and resulting temperature corrections for the HO_2 line strengths. The resulting combined strengths of the nearly coincident line pair at 1371.927 cm^{-1} were: 1.21×10^{-20} cm^2 at 274 K, 9.74×10^{-21} cm^2 at 333 K, and 8.49×10^{-21} cm^2 at 373 K. The results of the integrated line strength measurements (see equation II) were calibrated to peak absorption at each pressure and temperature employed, so that peak absorbance could be used as a proxy for total absorbance.

I_2 concentrations were monitored in the reaction cell via absorption spectroscopy near 500 nm. For these absorption

measurements, the arc lamp was used as the source of 500 nm radiation. After passing through the reaction cell but before entering the 0.22 m monochromator, the arc lamp beam was split and a small portion was directed into a 0.25 m monochromator (1.0 nm resolution; not shown in Figure 1) tuned to 500 nm. A photomultiplier tube at the monochromator output coupled to a picoammeter monitored the relative light level in the presence/absence of I_2. The concentrations of all other reagent gases were determined from their relative mass flow rates into the system, source concentrations, and the total system pressure. Temperature measurements in the gas flow through the reaction cell were performed using a 0.2 cm diameter copper−constantan thermocouple. The thermocouple was inserted into the cell through a vacuum-tight joint fitted to a Teflon disk, which was affixed to the cell in place of one of the magnesium fluoride windows. This allowed the position of the thermocouple to be varied along the length of the reaction cell. Conditions during the temperature measurements were set identical to those of the rate coefficient experiments. Temperature variations as a function of position in the gas flow through the cell were found to be less than 0.5 °C.

The gases used in this study had the following stated minimum purities: He 99.9999%, N_2 99.999%, O_2 99.99%, Cl_2 99.99%, SF_6 99.99%, I_2 99.99%, SO_2 99.98%, CH_3OH 99.9%, NO 99.0%; in the cases of Cl_2, SO_2, and SF_6, the stated purity refers to the liquid phase in the high-pressure gas cylinder. SF_6, N_2, NO, and O_2 were used as supplied. Cl_2, CH_3OH, and SO_2 were degassed repeatedly at 77 K and then diluted in N_2, and the resulting mixtures were stored in 12 L Pyrex bulbs. NO_2 was prepared by storing NO in a 12 L Pyrex bulb with a large excess of O_2, allowing the mixture to react. I_2 was introduced into the gas flow via a continuous regulated flow of N_2 which was maintained over crystalline I_2 to generate a dilute I_2/N_2 mixture.

Data Analysis

A chemical model was developed to describe the system behavior and analyze the observed concentration temporal profiles. To most efficiently describe the system chemistry, the model was divided into two temporal regions: $t \leq 55$ μs and $t > 55$ μs. Initially, the laser flash produces a large number of radical species, and the resulting chemistry is very complex. However, most of the radicals are converted to HO_2 or IO within 50 μs of the laser flash, greatly simplifying the system chemistry. It was found that a simplified chemical model could be used for the analysis after $t = 55$ μs without loss of integrity, as shown by direct comparison with the results of the complete model starting from $t = 0$. This simplified chemical model is given in Table 1. All rate coefficients in Table 1 are taken from the literature except the background loss rates for HO_2 and IO, which represent the effects of net diffusion of radicals out of the detection region and reactions with minor impurities in the gas mixture. The background loss rate for IO was estimated by observing IO loss in the absence of HO_2 for various IO concentrations, with special weight given to lower concentrations (which minimize the contribution from the IO + IO reaction). Comparison between the observed concentration profiles and simulations showed the contribution from background losses was small, and although no precise value could be derived, the value shown represents an estimate close to the observed upper limit. Because detection was not as sensitive for HO_2 as for IO, HO_2 loss could not be studied at low enough concentrations (and hence, slow enough HO_2 self-reaction loss rates) for the above procedure to give definitive results. Therefore, the HO_2 background loss rate was assumed to be the same as that found for IO. The overall error in k_3 introduced by uncertainties in the background radical loss rates is very small because (1) k_3 is sensitive to the absolute instantaneous value of $[HO_2]$ (which was measured directly) but not its time derivative, and (2) the IO background loss rate was much smaller than the loss rates due to reaction 3, which always exceeded 1500 s^{-1}.

TABLE 1: Reaction Mechanism for Modeling HO_2 + IO Temporal Profiles

reactants	products	k (cm^3 $molecule^{-1}$ s^{-1})[a]
IO + HO_2	all[b]	variable
IO + IO	all[b]	8.0×10^{-11}
IO + NO_2	$IONO_2$	4.9×10^{-13}
IO + NO	I + NO_2	2.0×10^{-11}
HO_2 + HO_2	H_2O_2 + O_2	1.7×10^{-12}
HO_2 + NO_2	HO_2NO_2	1.5×10^{-13}
HO_2 + NO	NO_2 + OH	8.1×10^{-12}
IO	background loss	25 s^{-1} [c]
HO_2	background loss	25 s^{-1} [c]

[a] All rate coefficients are 298 K values and are obtained from ref 11 unless otherwise indicated; rate coefficients for association reactions are 25 Torr values. [b] Because none of the products make important contributions to secondary production and/or loss of IO or HO_2, individual reaction channels were not specified in the mechanism. [c] Estimated (see text).

TABLE 2: Rate Coefficients for Modeling HO_2 + IO Temporal Profiles at Temperatures Other than 298 K

		k (cm^3 $molecule^{-1}$ s^{-1})[a]		
reactants	products	274 K	333 K	374 K
IO + IO	all[b]	9.0×10^{-11}	6.7×10^{-11}	5.7×10^{-11}
IO + NO_2	$IONO_2$	6.6×10^{-13}	2.7×10^{-13}	1.8×10^{-13}
IO + NO	I + NO_2	2.2×10^{-11}	1.9×10^{-11}	1.7×10^{-11}
HO_2 + HO_2	H_2O_2 + O_2	2.0×10^{-12}	1.4×10^{-12}	1.1×10^{-12}
HO_2 + NO_2	HO_2NO_2	1.6×10^{-13}	8.8×10^{-14}	6.2×10^{-14}
HO_2 + NO	NO_2 + OH	8.7×10^{-12}	7.4×10^{-12}	6.8×10^{-12}

[a] Temperature-dependent rate coefficients taken from ref 11; termolecular values shown for 25 Torr total pressure. [b] Because none of the products make important contributions to secondary production and/or loss of IO or HO_2, individual reaction channels were not specified in the mechanism.

Most of the reactions given in Table 1 have temperature-dependent rate coefficients. For analyzing the temperature-dependence data, the rate coefficients in the model were adjusted on the basis of values reported in the literature. A summary of the adjusted values is given in Table 2; all values are for 25 Torr total pressure.

Simulations demonstrate that once IO and HO_2 production are complete, HO_2 loss is due primarily to its self-reaction and reaction with NO_2. IO loss is dominated by reaction with HO_2, with contributions from reactions of IO with NO_2, NO, and IO accounting for 10−35% of IO loss rates, depending on experimental conditions. Under these conditions, the rate coefficient for IO + HO_2, k_3, and the HO_2 concentration temporal profile are the strongest determinants of the shape of the IO temporal profile. To find the experimental value for k_3, the differential equations describing the time rates of change of the chemical species in the simplified model (Table 1) were integrated numerically using exact experimental conditions while iteratively varying k_3 to achieve a best fit to the measured HO_2 and IO concentration temporal profiles; in this fitting procedure, k_3 was the *only* variable parameter.

As a result of differences in the HO_2 and IO measurement and data collection techniques, data collection could not be synchronized for both species at every point in time. For the inputs to the numerical integration routine, however, synchro-

nous HO_2 and IO data were required. Therefore, HO_2 concentrations at times intermediate to the measured values were inferred by interpolation along a smooth analytical function fit to the HO_2 data via nonlinear least-squares analysis. The function used was of the form $\exp(\ln(\alpha + 2\beta t)^{-1} + \gamma t)$, which is an approximation of the functional form of the decay temporal profile assuming the $HO_2 + HO_2$ and $HO_2 + NO_2$ reactions dominate. This approach was compared with other interpolation methods (data smoothing, polynomial spline) and judged superior. Residuals obtained from fits of the HO_2 data to the above functional form were always randomly distributed about zero over the entire time interval of interest for determination of k_3.

The analyses for deriving k_3 were performed using FACSIMILE (release 3.05, United Kingdom Atomic Energy Authority), a software package that performed the iterative fits to the data. Figure 5 shows the simulated decay temporal profiles of HO_2 and IO, respectively, resulting from the analysis of a typical experiment, along with the measured profiles for comparison. To demonstrate the sensitivity of the data to k_3, simulated temporal profiles that employed k_3 values somewhat higher and somewhat lower than the best fit value are also shown. Under the experimental conditions employed (i.e., $[HO_2] \gg [IO]$), the IO temporal profile provides a sensitive indicator of k_3, whereas the HO_2 temporal profile is relatively insensitive to k_3.

To determine the sensitivity of the results to variations in the input parameters, several analyses were performed in which the reactant concentrations and assumed rate coefficients were independently and systematically varied. The final value of k_3 was found to vary in approximately inverse proportion to the peak HO_2 concentration, as would be expected under truly pseudo-first-order conditions. Variations in [IO] that reflected a ±25% uncertainty in the 427.2 nm absorption cross section, on the other hand, produced a change of less than 1% in the resulting mean k_3 derived from the analysis. The rate coefficients for the reactions IO + IO, NO_2 + IO, and NO + IO were also simultaneously varied within the limits of their estimated uncertainties (±50%, ±30%, and ±20%, respectively [11]) to determine the potential contribution to the uncertainty in the value of k_3 (NO is formed along with $O(^3P_J)$ via NO_2 photolysis, i.e., reaction 9). In a typical room-temperature experiment at peak [IO], the contributions to the IO loss rate from each of the above reactions is IO + IO, 240 s^{-1}; NO_2 + IO, 215 s^{-1}; NO + IO, 20 s^{-1}. These reactions were found in combination to result in variations in the value of k_3 of between ±8% and ±15%, depending on experimental conditions (primarily HO_2 concentration, and to a lesser extent temperature). Finally, variations by factors of five (up or down) in the initial estimated value of k_3 input to the model had no effect on the value of k_3 to which the simulations ultimately converged.

Reactions 6−10 comprise the primary radical reactions involved in the generation of HO_2 and IO during the first 55 μs after the photolysis laser flash. Side reactions which generated other radical species also occurred on this short time scale, however. Most are of little consequence in determining the chemical evolution of the system; however, a few warrant detailed consideration for understanding the system chemistry on short time scales. One such side reaction is the Cl atom removal process

$$Cl(^2P_J) + I_2 \rightarrow ICl + I(^2P_J) \qquad (13)$$

which accounts for up to 17% of Cl atom loss. The fact that Cl atoms are titrated to generate HO_2 results in peak $[HO_2]$ slightly lower than would otherwise be generated. The products of reaction 13 are of insignificant consequence in subsequent chemistry.

Although reaction 10 is the dominant O atom reaction pathway, approximately 3% of O atoms react with HO_2 to produce OH via

$$O(^3P_J) + HO_2 \rightarrow OH + O_2 \qquad (14)$$

The OH thus produced reacts with I_2 to produce HOI and I atoms and to a much lesser extent with CH_3OH to generate water and CH_2OH, the latter of which generates HO_2 as described above.

TABLE 3: Summary of the Experimental Results at T = 298 K

		concentrations[a] (10^{13} cm^{-3})						k_3 (10^{-11} cm^3 molecule^{-1} s^{-1})
expt	P (Torr)	Cl_2	NO_2	I_2	CH_3OH	$HO_{2\,max}$	IO_{max}	
1	25	234	53.4	36.8	1080	2.79	0.29	10.51
2	25	282	57.6	38.8	1060	3.51	0.37	9.61
3	25	304	54.2	39.0	1080	3.59	0.22	10.69
4	25	205	53.6	38.3	1070	2.58	0.29	9.55
5	25	152	52.1	43.9	1030	1.91	0.30	10.52
6	25	202	53.3	43.9	1050	2.49	0.30	10.33
7	25	350	65.0	43.9	1050	4.01	0.33	9.84
8	25	392	64.6	44.8	1080	4.50	0.34	8.63
9	25	441	64.7	44.8	1060	4.87	0.36	9.21
10	25	506	64.4	44.8	1090	5.49	0.37	9.33
11	25	580	64.6	44.8	1090	6.44	0.34	8.50
12	25	288	53.2	51.5	1010	3.55	0.29	9.59
13	25	468	54.4	51.5	1030	4.98	0.30	9.81
14	25	371	52.5	51.5	1020	4.31	0.30	10.10
15	25	410	52.0	40.2	1310	4.62	0.29	10.08
16	25	355	51.3	40.2	1330	3.96	0.30	9.76
17	25	309	51.6	40.2	1330	3.43	0.31	9.71
18	25	500	52.1	41.6	750	5.34	0.29	9.42
19	25	290	52.7	41.6	790	3.16	0.30	9.67
20	25	451	51.8	41.6	780	4.41	0.30	10.42
21	12	472	51.4	43.8	1010	5.56	0.29	9.94
22	12	157	51.8	43.8	1020	1.94	0.31	9.77
23	12	268	51.2	43.8	972	3.43	0.30	9.51
24	12	318	52.0	43.8	987	4.21	0.31	9.38

[a] The concentration of O_2 was 1.0×10^{17} molecules cm^{-3}, and the concentration of SF_6 was 3×10^{16} molecules cm^{-3} in all experiments.

Results and Discussion

The exact conditions used in all experimental runs used to obtain the value for k_3 are given in Tables 3 and 4, along with the resulting rate coefficient derived from each. An unweighted average of the values obtained from individual experiments at 298 K gives $k_3 = (9.7 \pm 1.0) \times 10^{-11}$ cm^3 molecule^{-1} s^{-1} where the uncertainty is 2σ and represents precision only. An additional large source of error is due to the uncertainty in the room-temperature line strength for HO_2 at 1372 cm^{-1}. When this is combined with estimates of other potential sources of systematic error (discussed above), one obtains k_3(298 K) = $(9.7 \pm 2.9) \times 10^{-11}$ cm^3 molecule^{-1} s^{-1}. The temperature dependence of the reaction is described by the Arrhenius expression $k_3 = (9.3 \pm 3.3) \times 10^{-12} \exp(680 \pm 110/T)$, where the quoted uncertainties are the standard deviations in the slope and intercept of a ln k vs T^{-1} fit of the data (see Figure 6). The average values determined at each temperature are summarized in Table 5.

The uncertainties given in the above Arrhenius expression do not provide a very good indication of how the uncertainty in k_3 varies as a function of temperature; a reasonable approach for specifying this uncertainty parameter is to employ the following relationship:[11]

TABLE 4: Summary of Experimental Results at Temperatures Other Than 298 K

		concentrations[a] (10^{13} cm^{-3})						k_3 (10^{-11} cm^3
expt	T (K)[b]	Cl_2	NO_2	I_2	CH_3OH	$HO_{2\,max}$	IO_{max}	molecule^{-1} s^{-1})
25	274	387	63.9	28.2	1240	5.09	0.16	12.49
26	274	230	57.5	28.2	1220	3.15	0.22	9.82
27	274	308	58.9	28.2	1160	4.16	0.21	9.57
28	274	482	65.7	28.2	1220	6.21	0.18	11.48
29	274	193	58.2	28.2	1230	2.62	0.21	10.56
30	274	595	66.2	28.2	1220	6.83	0.18	10.89
31	274	684	64.3	28.2	1220	7.29	0.19	11.79
32	274	349	65.4	28.2	1230	4.64	0.20	9.68
33	333	323	81.5	40.6	1160	3.29	0.38	5.31
34	333	245	82.0	40.6	1160	2.66	0.46	6.08
35	333	489	81.0	40.6	1140	5.33	0.34	6.34
36	333	416	81.1	40.6	1140	4.54	0.50	6.85
37	333	365	82.2	40.6	1150	3.84	0.54	6.99
38	333	548	83.1	40.6	1140	5.39	0.49	7.97
39	333	281	81.4	40.6	1150	2.96	0.51	6.82
40	333	317	82.3	40.6	1140	3.34	0.50	6.79
41	373	323	109	41.2	1070	3.14	0.44	6.48
42	373	493	109	41.2	1060	4.56	0.37	5.60
43	373	372	106	41.2	1190	3.35	0.35	5.80
44	373	615	105	41.2	1170	5.49	0.33	5.97
45	373	426	105	41.2	1160	3.73	0.43	6.43
46	373	695	106	41.2	1150	6.02	0.39	4.97
47	373	559	105	41.2	1140	5.18	0.44	6.57
48	373	772	97.7	35.1	1090	7.01	0.32	5.44

[a] The concentration of O_2 was 1.0×10^{17} molecules cm^{-3}, and the concentration of SF_6 was 3×10^{16} molecules cm^{-3} in all experiments. [b] The pressure was 25 Torr in all experiments.

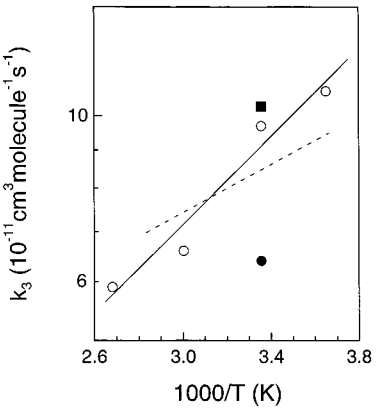

Figure 6. Arrhenius plot for the HO_2 + IO reaction. The solid line is obtained from a least-squares analysis of our data (open circles) and represents the Arrhenius expression 9.3×10^{-12} exp(680/T) cm^3 molecule^{-1} s^{-1}. The dashed line is obtained from the unpublished data of Knight and Crowley (ref 14). The solid circle is the 298 K rate coefficient reported by Jenkin et al. (ref 7), and the solid square is the 298 K rate coefficient reproted by Maguin et al. (ref 8).

TABLE 5: Summary of HO_2 + IO Rate Coefficients as a Function of Temperature

T (K)	no. of exps	av k (10^{-11} cm^3 molecule^{-1} s^{-1})[a]
274	8	10.8 ± 1.0
298	24	9.7 ± 1.0
333	8	6.6 ± 1.4
373	8	5.9 ± 1.0

[a] Uncertainties are 2σ and represent precision only.

$$f(T) = f(298)\exp\left[\left|\frac{\Delta E}{R}\left(\frac{1}{T} - \frac{1}{298}\right)\right|\right] \qquad \text{(V)}$$

In equation V, $f(T)$ and $f(298)$ are uncertainty factors in the rate coefficient at temperatures T and 298 K, respectively, and $\Delta E/R$ is an estimated uncertainty in E_a/R ($E_a \equiv$ the experimental activation energy). As discussed above, $f(298) \approx 1.3$. Choosing $\Delta E/R = 150$ K gives the reasonable uncertainty factors $f(274) \approx 1.36$ and $f(374) \approx 1.44$ at the high- and low-temperature limits of our study.

There are two previously reported measurements of k_3(298 K) in the literature. The present result at room temperature is in excellent agreement with a study by Maguin et al.[8] that experimentally determined the rate coefficient to be $(1.03 \pm 0.13) \times 10^{-10}$ cm^3 molecule^{-1} s^{-1} using a discharge-flow/mass spectrometry technique but 50% faster than that reported by Jenkin et al.,[7] who measured a value of $(6.4 \pm 0.7) \times 10^{-11}$ cm^3 molecule^{-1} s^{-1} using molecular modulation to produce radicals in a $CH_3OH/I_2/O_3/O_2$/Ar mixture (760 Torr) and UV/visible absorption spectroscopy to monitor the time-dependent behavior of the radicals. There are no literature reports of k_3 at temperatures other than 298 K. Both previous studies were performed with HO_2 in approximately 10-fold or greater excess over IO, although Jenkin et al. employed a more limited range of conditions than either Maguin et al. or this study. Maguin et al. suggested that if reaction 3b (see below) is a significant channel, I and OH would be instantly converted back to IO and HO_2 in the reaction mixture employed by Jenkin et al. (via reaction with O_3), possibly explaining the slower rate coefficient reported by Jenkin et al. (reaction 3b would not affect the HO_2 or IO temporal profiles in this study). Vibrationally excited states of IO were found to be a potential problem using 427.2 nm detection in this study and were therefore deactivated rapidly by the addition of SF_6; their fate in Ar is not well-known. Detection of HO_2 by UV absorption is subject to interferences from other absorbers produced in side reactions (H_2O_2, for instance).

An unpublished temperature-dependence study of reaction 3 has recently been performed by workers at the Max Planck Institute in Mainz, Germany using a discharge-flow reactor with mass spectrometric detection of IO;[14] preliminary results appear to be in good agreement with the present study over the temperature range of overlap between the two.

Reaction 3 has four potentially energetically accessible reaction channels:

$$HO_2 + IO \rightarrow HOI + O_2 \qquad \text{(3a)}$$

$$\rightarrow OH + I(^2P_J) + O_2 \qquad \text{(3b)}$$

$$\rightarrow HI + O_3 \qquad \text{(3c)}$$

$$\rightarrow HO_2{\cdot}IO \qquad \text{(3d)}$$

Although significant uncertainties exist in the heats of formation of HOI and IO, channels 3b and 3c are probably endothermic[11,15] and therefore would not be expected to be important at the temperatures investigated in this study. Maguin et al.[8] detected HOI as a primary reaction product, and although they could not determine a branching ratio, failure to detect O_3 argues against the importance of channel 3c. Further studies are needed to determine the branching ratios for reaction 3.

Because HOI is likely to be a major product of the IO + HO_2 reaction, one potential kinetic complication which needs to be considered is IO regeneration via the secondary reaction

$$HO_2 + HOI \rightarrow H_2O_2 + IO \qquad \text{(15)}$$

Although there are no kinetic data available in the literature for reaction 15, it seems safe to assume that this reaction is unimportant, i.e., that $k_{15} \ll k_3$, because the best available

thermochemistry[11,16] suggests that reaction 15 is endothermic by 31 ± 14 kJ mol^{-1}.

Maguin et al.[8] speculate that the reaction mechanism for the HOI formation channel involves H atom transfer (I−O···H−O−O), citing the high rate coefficient as rationale. The finding of a negative activation energy in this study, however, argues in favor of a long-range attractive interaction between IO and HOO•, which suggests that reaction occurs via initial IO attack on the radical site in HOO•. The HO_2 + XO (X = Cl, Br, I) reactions all appear to have negative activation energies, with the 298 K rate coefficients increasing as X is substituted in the order Cl < Br < I.[11] This pattern could be attributable to increasing tendency of the larger XO species to access the available triplet surfaces through spin-orbit coupling.[17] The HO_2 + BrO reaction probably proceeds via formation of HOOBrO and subsequent formation of a cyclic intermediate that decomposes to HOBr + O_2;[9,18] this is also the likely mechanism for the HO_2 + ClO reaction.[18] Ab initio calculations by Francisco and co-workers[19,20] show that the $HClO_3$ isomers have the same energy ordering as those for $HBrO_3$. These patterns suggest the same mechanism for HO_2 + IO. The $HBrO_3$ isomer HOOOBr is thought to be quite stable,[19] suggesting that the analogous species HOOOI may also be relatively strongly bound. The species HOOOI could dissociate to HI + O_3 via a cyclic intermediate but, as discussed above, this pathway does not apppear to be energetically favorable. Hence, HOOOI warrants consideration as a potential reaction product, particularly at upper tropospheric and lower stratospheric temperatures. Ab initio calculations of the structures and energetics of the HIO_3 isomers would be helpful in assessing this possibility, as well as the stabilities of all potential products of channel 3d.

Because reaction 3 is the rate-determining step in the ozone destruction cycle involving reactions 2−5, it is of importance in determining the potential role of iodine in ozone chemistry in the atmospheric regions where IO_x and HO_x levels are reasonably high. These include the marine boundary layer, where concentrations of the source gas CH_3I have been measured at between 1 and 50 pptv,[21,22] the middle and upper tropical troposphere,[3] and possibly the lower stratosphere.[4] Davis et al.[3] used recently available data to calculate the effects of the iodine cycles involving reaction 3 and the IO + IO reaction as the rate-limiting steps for various CH_3I mixing ratios. These workers found that inclusion of iodine chemistry (assuming 7 pptv total reactive iodine) could increase total tropospheric column ozone loss by as much as 30% and reduce HO_2/OH ratios 18−24% depending on altitude and latitude; their model assumed a value of $k_3 = 8.4 \times 10^{-11}$ cm^3 $molecule^{-1}$ s^{-1}. A higher rate coefficient would increase both of these effects, especially at higher altitudes given the temperature dependence found here. Solomon et al.[4] assumed $k_3 = 6.4 \times 10^{-11}$ cm^3 $molecule^{-1}$ s^{-1} in their assessment of the potential role of iodine in stratospheric ozone loss; the present result indicates the rate coefficient is probably 3 times faster at lower stratospheric temperatures. Moreover, the relative importance of the HO_2 cycle in any iodine-mediated stratospheric ozone loss is greater than Solomon et al.[4] concluded because the IO + ClO rate coefficient was recently measured to be 5 times slower at stratospheric temperatures than their analysis assumed.[23]

Because HOI photolysis leading to OH formation occurs rapidly in the troposphere, reaction 3 effectively supplements other processes which convert HO_2 to OH, primarily reaction with NO. It is therefore interesting to compare the HO_2-to-OH conversion rates from reaction 3 with those due to the reaction

$$HO_2 + NO \rightarrow OH + NO_2 \qquad (16)$$

in atmospheric environments where reactive iodine is likely to be significant. Measurements in the tropical and midlatitude Western Pacific during the September−October 1991 Western Pacific Exploratory Mission A (PEM-West A)[3,24] allow such a comparison for various altitudes in atmospheric environments influenced largely by marine sources. In the tropical Western Pacific, CH_3I measurements show mean mixing ratios of 0.6 pptv from near the surface to the top of the boundary layer, dropping gradually to 0.1 pptv near the tropopause, leading to estimated total reactive iodine I_x (I_x = I + IO + HI + HOI + $2I_2O_2$ + INO_x) mixing ratios of 0.3−0.5 pptv, respectively;[3] I_x concentrations would be higher in the presence of multiple source gases, a more likely scenario. Davis et al.[3] proposed I_x values in the range 1.5−7 pptv as reasonable possibilities. PEM-West A measurements of NO show mixing ratios in the tropics of 0−10 pptv (mean ≃2 pptv) in the boundary layer, rising gradually to 10−50 pptv (mean ≃ 20 pptv) in the upper free troposphere. At a temperature of 300 K the ratio of the rate coefficients k_3/k_{16} is 12 (using our results for HO_2 + IO and the DeMore et al. recommendation[11] for HO_2 + NO), leading to ratios of the total IO/NO conversion rates of 9−42 over the range of estimated I_x concentrations in the boundary layer at the measured mean NO concentration (2 pptv). At a temperature of 230 K, k_3/k_{16} rises to 17, leading to IO/NO conversion rate ratios of 1−6 for mean NO above 10 km (20 pptv). In the midlatitude Western Pacific, NO measurements showed mixing ratios ranging from 0 to 10 pptv in the boundary layer (mean ≃ 2 pptv) to 40−200 pptv at 11 km (mean ≃ 100 pptv). CH_3I measurements averaged 1.0 pptv in the boundary layer, dropped to near 0.1 pptv in the middle troposphere, and rose again to nearly 0.5 pptv at an altitude of 11 km. Using the same total I_x estimates as for the PEM-West A tropics, the IO/NO conversion rate ratio in the midlatitude measurement region is in the same range in the boundary layer as for the tropics but drops to 0.25−1 at 11 km. On the basis of the above discussion, it seems likely that the HO_2 + IO reaction exerts an important influence on the OH/HO_2 concentration ratio in the troposphere.

Acknowledgment. This research has been supported through Grant NAG5-3634 from the National Aeronautics and Space Administration−Upper Atmosphere Research Program. We thank John Crowley and Gary Knight for communicating their results to us prior to publication.

References and Notes

(1) Chameides, W. L.; Davis, D. D. *J. Geophys. Res.* **1980**, *85*, 7383.
(2) Jenkin, M. E. A comparative assessment of the role of iodine photochemistry in tropospheric ozone depletion. In *The Tropospheric Chemistry of Ozone in the Polar Regions*; Niki, H., Becker, K. H., Eds.; NATO ASI Ser. Vol. 17, Springer-Verlag: New York, 1993.
(3) Davis, D. D.; Crawford, J.; Liu, S.; McKeen, S.; Bandy, A.; Thornton, D.; Rowland, F.; Blake, D. *J. Geophys. Res.* **1996**, *101*, 2135.
(4) Solomon, S.; Garcia, R. R.; Ravishankara, A. R. *J. Geophys. Res.* **1994**, *99*, 20491.
(5) Kritz, M. A.; Rosner, S. W.; Kelley, K. K.; Loewenstein, M.; Chan, K. R. *J. Geophys. Res.* **1993**, *97*, 8725.
(6) Danielsen, E. F. *J. Geophys. Res.* **1993**, *98*, 8665.
(7) Jenkin, M. E.; Cox, R. A.; Hayman, G. D. *Chem. Phys. Lett.* **1991**, *177*, 272.
(8) Maguin, F.; Laverdet, G.; Le Bras, G.; Poulet, G. *J. Phys. Chem.* **1992**, *96*, 1775.
(9) Cronkhite, J. M.; Stickel, R. E.; Nicovich, J. M.; Wine, P. H. *J. Phys. Chem. A* **1998**, *102*, 6651.
(10) Harwood, M. H.; Burkholder, J. B.; Hunter, M.; Fox, R. W.; Ravishankara, A. R. *J. Phys. Chem. A* **1997**, *101*, 853.
(11) DeMore, W. B.; Sander, S. P.; Golden, D. M.; Hampson, R. F.; Kurylo, M. J.; Howard, C. J.; Ravishankara, A. R.; Kolb, C. E.; Molina,

M. J. *Chemical Kinetics and Photochemical Data for Use in Stratospheric Modeling*; Evaluation No. 12, Jet Propulsion Laboratory Publication No. 97-4, 1997.

(12) Zahniser, M. S.; McCurdy, K. E.; Stanton, A. C. *J. Phys. Chem.* **1989**, *93*, 1065.

(13) Rothman, L. S.; Schroeder, J.; McCann, A.; Gamache, R. R.; Wattson, R. B.; Flaud, J.-M.; Perrin, A.; Dana, V.; Mandin, J.-Y.; Goldman, A.; Massie, S.; Varanasi, P.; Yoshino, K. *J. Quant. Spectrosc. Radiat. Transfer* (to be published).

(14) Knight, G.; Crowley, J., manuscript in preparation.

(15) Berry, R. J.; Yuan, J.; Misra, A.; Marshall, P. *J. Phys. Chem A* **1998**, *102*, 5182.

(16) Hassanzadeh, P.; Irikura, K. K. *J. Phys. Chem. A* **1997**, *101*, 1580.

(17) Bogan, D. J.; Thorn, R. P.; Nesbitt, F. L.; Stief, L. J. *J. Phys. Chem.* **1996**, *100*, 14383.

(18) Li, Z.; Friedl, R. R.; Sander, S. P. *J. Chem. Soc., Faraday Trans.* **1997**, *93*, 2683.

(19) Guha, S.; Francisco, J. S. *J. Phys. Chem. A* **1998**, *102*, 2072.

(20) Francisco, J. S.; Sander, S. P. *J. Phys. Chem.* **1996**, *100*, 573.

(21) Reifenshauser, W.; Heumann, K. G. *Atmos. Environ.* **1992**, *26(A)*, 2905.

(22) Oram, D. E.; Penkett, S. A. *Atmos. Environ.* **1994**, *28*, 1159.

(23) Turnipseed, A. A.; Gilles, M. K.; Burkolder, J. B.; Ravishankara, A. R. *J. Phys. Chem. A* **1997**, *101*, 5517.

(24) Singh, H. B.; Herlth, D.; Kolyer, R.; Salas, L.; Bradshaw, J. D.; Sandholm, S. T.; Davis, D. D.; Crawford, J.; Kondo, Y.; Koike, M.; Talbot, R.; Gregory, G. L.; Sachse, G. W.; Browell, E.; Blake, D. R.; Rowland, F. S.; Newell, R.; Merrill, J.; Heikes, B.; Liu, S. C.; Crutzen, P. J.; Kanakidou, M. *J. Geophys. Res.* **1996**, *101*, 1793.